Technical Report PAR-10021867-092020-4

Tabular models for high pressure and high strain-rate granular plasticity

Biswajit Banerjee
Parresia Research Limited, Auckland, New Zealand
b.banerjee.nz@gmail.com

David M. Fox
CCDC Army Research Laboratory, Aberdeen Proving Ground, MD, USA
david.m.fox1.civ@mail.mil

Richard A. Regueiro
University of Colorado, Boulder, CO, USA
richard.regueiro@colorado.edu

Saturday, December 12, 2020

Abstract

Experiments and micromechanical simulations generate tabular data for material behavior. Typically, models are fit to these material data before engineering simulations can be performed. It is frequently discovered that existing models cannot express the experimental data adequately, and new models have to be developed and fit. This process is undesirable and a preferable approach is to directly use the tabular data without model building. In this work, we discuss such a tabular model and associated numerical algorithms in the context of the elastoplastic behavior of a poorly graded concrete sand. Special considerations for tabulated data are described and the model is tested in hydrostatic compression, uniaxial compression, and pure shear. The model reproduces experimental behavior of the sand, but only if the bulk moduli and crush curve extracted from the input hydrostat are scaled by 1.7 and 1.2 times, respectively. An implication of this observation is that the assumption of isotropy may be significantly inaccurate at high compression.

1 Introduction

Tabulated data are increasingly being used as inputs to elastoplastic simulations to avoid the development of specific models that fit those data. However, algorithms that can handle such data are sparsely described in the research literature. In this work we describe an algorithm that can be used to handle tabulated data for elastoplastic materials that are pressure-dependent and have a compression cap, but *do not* depend on the third principal invariant of the deviatoric stress (J_3). The material that is explored is a poorly-graded concrete sand that not only is nonlinear in the elastic domain, but also exhibits a strong increase of the elastic bulk modulus with increasing inelastic strain. We

are mainly interested in the moderate to extremely high pressure regimes that are experienced in applications such as the penetration of soil by high-speed projectiles and explosions in soil.

In previous work, we have explored the use of support vector models (Banerjee, Fox, and Regueiro, 2020c) and neural network models (Banerjee, Fox, and Regueiro, 2020b) to generate functional representations of multi-variable tabular data for elastoplastic simulations. If the extra effort of fitting such machine learning models is to be avoided, tabular data have to be interpolated directly. Various approaches to interpolating tabular data, e.g., linear interpolation, radial basis function interpolation, and kriging interpolation have been discussed in Banerjee, Fox, and Regueiro (2020a). In this paper, we focus on the elastoplasticity algorithm and use linear interpolation of tabular data (with the understanding that any of the other approaches can be swapped in for linear interpolation in the elastoplasticity code).

The basics of elastoplasticity theory in rate form are discussed, with emphasis on elasto-plastic coupling and the contribution of the coupling tensor ($\boldsymbol{Z}$) and the projection tensor ($\boldsymbol{P}$). The stress update algorithm requires a closest-point projection step because the yield condition is only available in discretized form and only the zero level set of the yield function is available when tabular data are used directly. An iterative process is used to improve estimates of the projection tensor ($\boldsymbol{P}$) and the non-hardening plastic strain rate factor ($\dot{\lambda}$). A hardening correction is then applied to allow for the evolution of the compression cap.

Several special considerations are needed to handle tabular data. For example, the input yield function data have to be forced to lie on a convex surface. Also, the vertices created during the discretization of the yield function have to be smoothed. We use a quadratic B-spline for smoothing the yield surface and use that smooth approximation to determine the closest point and normal to the yield surface for a give trial stress state. The model and algorithms have been implemented in the open-source Vaango code and tested for accuracy using hydrostatic compression, uniaxial compression, and simple shear. Results from these simulations are compared with hydrostatic compression loading-unloading data and show that the approach discussed in this work is both computationally efficient and accurate.

This paper is organized as follows. Section 2 discusses the experimental data that provides the justification for this work as well as a validation set. The elastoplasticity model is discussed in Section 3 and the stress update algorithm in elaborated upon in Section 4. Special considerations that are needed to handle tabular data are discussed in Section 5. The response of the model in hydrostatic compression is compared with experimental data in Section 6 and predicted behaviors in uniaxial tension and simple shear are presented. Some concluding remarks are given in Section 7.

2 Experimental data

The experimental data that have been used as a test-bed for the modeling process are for a dry, poorly-graded, concrete sand described by Fox et al. (2014) and tested at the University of Maryland.[1] Further details on the particular set used in this work can be found in (Banerjee, Fox, and Regueiro, 2020c). In this paper, compressive states are assigned positive values and tensile states are assigned negative values.

[1] Stephen Akers, 2018, Private communication, CCDC Army Research Laboratory, Aberdeen Proving Ground, MD, USA

The hydrostatic loading-unloading data for that sand is presented as a plot of pressure (p) as a function of the total volumetric strain (ε_v) in Figure 1(a). The loading curve, shown in cyan, is used to fit a crush-curve model. The unloading curves are used to fit a bulk modulus model that depends on the plastic strain. Tangents to the unloading curves represent the bulk modulus and have been plotted in Figure 1(b). There is a strong dependence of the bulk modulus (K) on both the elastic (ε_v^e) and plastic (ε_v^p) volumetric strains.

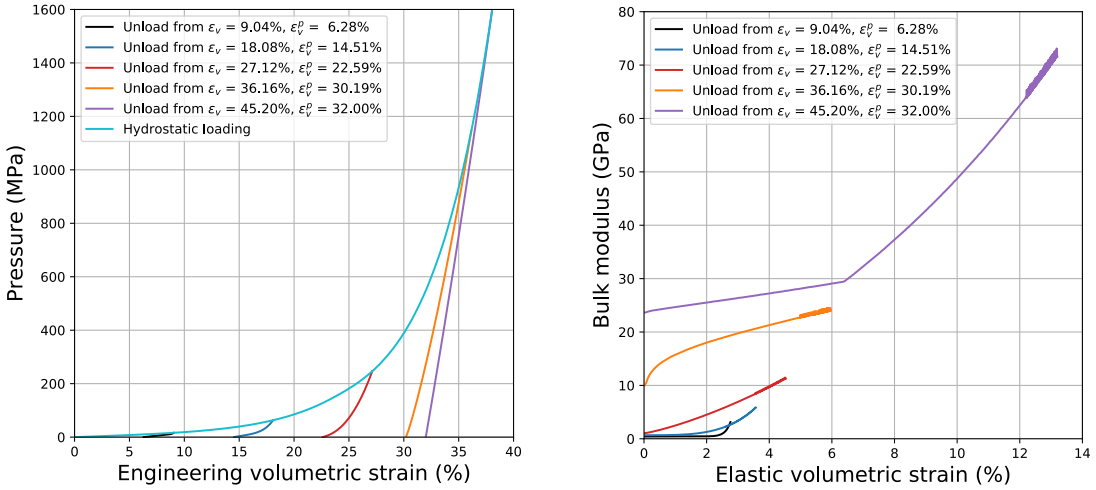

(a) Loading-unloading curves

(b) Tangent bulk modulus curves

Figure 1 – *Hydrostatic loading-unloading data and unloading bulk moduli for dry poorly-graded concrete sand.*

The crush-curve extracted from the hydrostatic compression data is depicted in Figure 2(a). Since the term "crush-curve" is used more commonly to refer to the change in porosity as a function of pressure form, we shown this form of the curve in Figure 2(b). The porosity (ϕ) has been computed using $\phi = p_3 - \varepsilon_p^v$ where ε_p^v is the volumetric plastic strain and $p_3 = 0.325$ is the volumetric plastic strain at which all pores have been crushed (Brannon, Fuller, et al., 2015).

The original yield function curve for the concrete sand intersected the deviatoric stress axis approximately 5 kPa (compression), indicating that a purely elastic response was not possible when the sand was loaded from zero strain. To ensure that simulations did not run into any difficulty, the function was shifted to the tensile regime by 5 kPa to provide a small amount of cohesion. A plot of the yield function in p-q space is shown in Figure 3. Here p is the mean stress, defined as $p = 1/3\,\mathrm{tr}(\boldsymbol{\sigma})$, q is the deviatoric yield stress given by $q = \sqrt{3J_2}$ where $J_2 = 1/2\,\mathbf{s} : \mathbf{s}$, $\boldsymbol{\sigma}$ is the Cauchy stress, $\mathbf{s} = \boldsymbol{\sigma} - p\boldsymbol{I}$ is the deviatoric part of the Cauchy stress, and $\boldsymbol{I}$ is the second-order identity tensor. The crush curve suggests that nonlinear bulk moduli are not sufficient to explain the observed yield response and a compression cap is needed to model the material.

3 Tabular elastoplasticity model

In this work, instead of designing algebraic expressions that can explain and fit the experimental data presented in Section 2, we use the tabular data directly in an elastoplasticity model. Models are, of

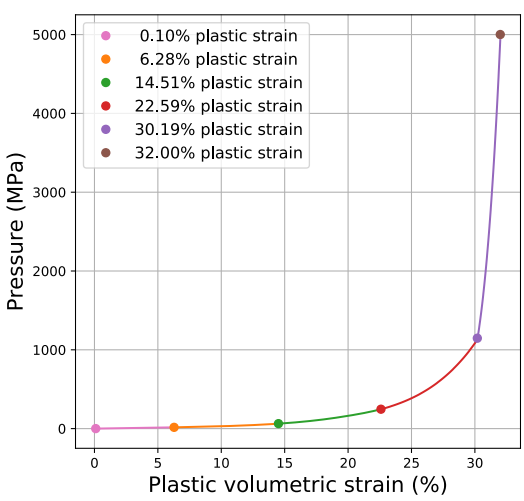

(a) Pressure crush-curve.

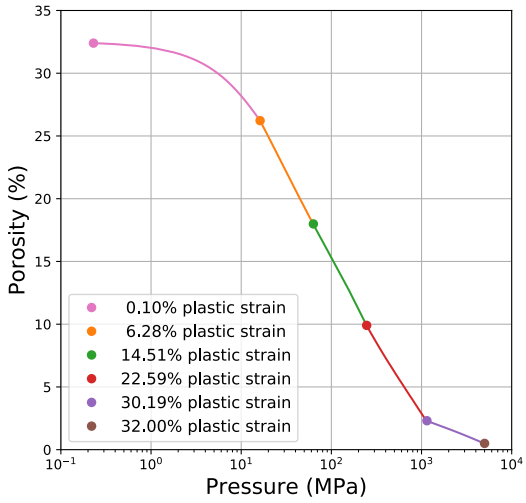

(b) Porosity crush-curve.

Figure 2 – *Crush-curves for dry poorly-graded concrete sand.*

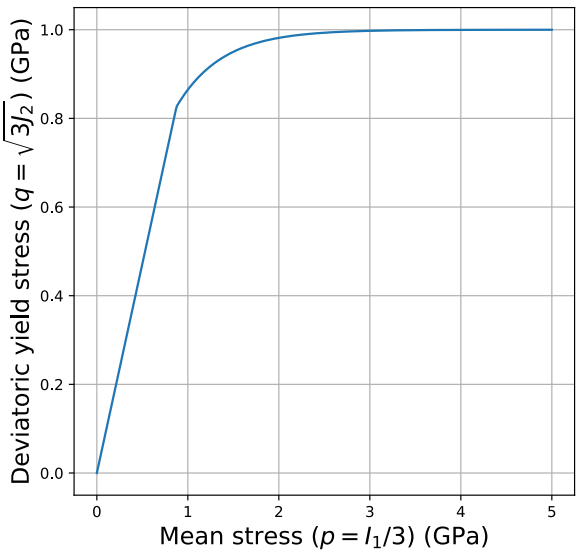

Figure 3 – *Yield function for dry poorly-graded concrete sand.*

course, needed where limited or no experimental data are available, such as for the evolution of the shear modulus and the compression cap for the yield surface.

We assume that the unrotated total strain rate ($\dot{\boldsymbol{\varepsilon}}$) can be additively decomposed as (Brannon, 2007; Banerjee and Brannon, 2019)

$$\dot{\boldsymbol{\varepsilon}} = \dot{\boldsymbol{\varepsilon}}^e + \dot{\boldsymbol{\varepsilon}}^p \tag{1}$$

where $\boldsymbol{\varepsilon}^e$ is the elastic strain and $\boldsymbol{\varepsilon}^p$ is the plastic strain. The unrotated nonlinear elastic response is assumed to be coupled with the plastic response and is given by a relation of the form

$$\boldsymbol{\sigma} = \boldsymbol{\sigma}(\boldsymbol{\varepsilon}^e, \varepsilon_v^p) \tag{2}$$

where $\boldsymbol{\sigma}$ is the unrotated Cauchy stress, and ε_v^p is the plastic volumetric strain defined as

$$\varepsilon_v^p := \int \operatorname{tr}(\dot{\boldsymbol{\varepsilon}}^p)\, dt\,. \tag{3}$$

The rate form of (2) is

$$\dot{\boldsymbol{\sigma}} = \frac{\partial \boldsymbol{\sigma}}{\partial \boldsymbol{\varepsilon}^e} : \dot{\boldsymbol{\varepsilon}}^e + \frac{\partial \boldsymbol{\sigma}}{\partial \varepsilon_v^p} \dot{\varepsilon}_v^p\,. \tag{4}$$

3.1 Elasticity model

The elastic response is assumed to be given by

$$\frac{\partial \boldsymbol{\sigma}}{\partial \boldsymbol{\varepsilon}^e} = \mathbf{C}(\varepsilon_v^e, \varepsilon_v^p) \tag{5}$$

where $\mathbf{C}$ is the elastic stiffness, assumed isotropic in this work, obtained by varying $\boldsymbol{\sigma}$ while keeping ε_v^p fixed, and $\varepsilon_v^e := \operatorname{tr}(\boldsymbol{\varepsilon}^e)$ is the volumetric elastic strain. The stiffness matrix can then be expressed as

$$\mathbf{C} = \left[K(\varepsilon_v^e, \varepsilon_v^p) - \tfrac{2}{3} G(\varepsilon_v^e, \varepsilon_v^p)\right] \boldsymbol{I} \otimes \boldsymbol{I} + 2G(\varepsilon_v^e, \varepsilon_v^p)\, \mathbf{I} \tag{6}$$

where K is the tangent bulk modulus, G is the tangent shear modulus, $\boldsymbol{I}$ is the second-order identity tensor, $\mathbf{I}$ is the symmetric fourth-order identity tensor.

In the tabular model, the tangent bulk modulus is determined from a table of unloading curves (see Figure 1 for an example). The unloading curves consist of data for the mean stress (pressure), $p = 1/3\operatorname{tr}(\boldsymbol{\sigma})$, as a function of the total engineering volumetric strain, ε_v. Each unloading curve is associated with a fixed plastic volumetric strain (ε_v^p). As discussed in Banerjee, Fox, and Regueiro (2020a), bulk moduli can either be computed by converting the pressure curves, $p(\varepsilon_v^p, \varepsilon_v^e)$, to bulk modulus curves, $K(\varepsilon_v^p, \varepsilon_v^e) = dp/d\varepsilon_v^e$, and interpolating the bulk moduli directly, or by interpolating pressures and computing bulk moduli using a central difference scheme:

$$K(\varepsilon_v^p, \varepsilon_v^e) = \frac{p(\varepsilon_v^p, \varepsilon_v^e + \epsilon) - p(\varepsilon_v^p, \varepsilon_v^e - \epsilon)}{2\epsilon} \tag{7}$$

where $\epsilon > 0 \in \mathbb{R}$. The tolerance ϵ is usually has a value of 10^{-6} or smaller.

The shear modulus is assumed to be either a constant (G_0) or determined using a constant Poisson's ratio (ν) from the bulk modulus, i.e.,

$$G(\varepsilon_v^p, \varepsilon_v^e) = \begin{cases} \frac{3K(1-2\nu)}{2(1+\nu)} & \text{if} \quad \nu \in [-1, 0.5] \\ G_0 & \text{otherwise} \end{cases} \tag{8}$$

3.2 Plasticity model

The yield function is assumed to be of the form

$$f = \sqrt{J_2} - g(p)\, F_c(p) \tag{9}$$

where $J_2 = 1/2\mathbf{s} : \mathbf{s}$ is the second principal invariant of the unrotated deviatoric Cauchy stress ($\boldsymbol{\sigma}$), and the deviatoric stress is $\mathbf{s} = \boldsymbol{\sigma} - p\boldsymbol{I}$. The function $g(p)$ is the deviatoric yield stress, assumed to be available in tabular form, while $F_c(p)$ is the compression cap. For elastic loading/unloading, $f < 0$. During plastic deformation $f = 0$. Values greater than zero are not allowed, though they are useful for stress update algorithms. This is expressed as the consistency condition, $\dot{f} = 0$.

Since tabular data for the cap are typically not available, we assume an elliptical function (Brannon, Fuller, et al., 2015):

$$F_c^2 = \begin{cases} 1 - \left(\frac{p-\kappa}{p_c-\kappa}\right)^2 & \text{for} \quad p \geq \kappa \\ 1 & \text{for} \quad p < \kappa \end{cases} \tag{10}$$

The value of κ is determined by the location of the compression cap (p_c) and a cap ratio (R) using

$$\kappa = p_t + R(p_c - p_t) \tag{11}$$

where p_t is the maximum tension that can be supported by the material, determined as the intersection of $g(p)$ with the mean stress axis (see Figure 3). A schematic of the two components of the yield function is shown in Figure 4.

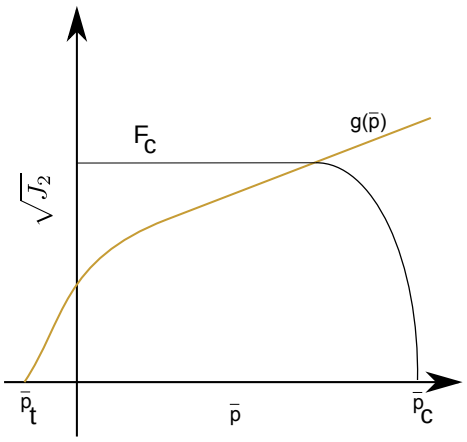

Figure 4 – *Schematic of the yield functions $g(\bar{p})$ and F_c. The notation $\bar{p}$ is used to facilitate comparisons with previous work. Note that $\bar{p} = -p$ when the convention is that tension is positive.*

The crush curve table (see Figure 2) is used to determine the location of maximum value of the compression cap (p_c) for a given value of ε_v^p. One-dimensional linear interpolation is used to extract the value of p_c for a given volumetric plastic strain.

The tabular model assumes a flow rule of the form

$$\dot{\boldsymbol{\varepsilon}}^p = \dot{\lambda}\boldsymbol{M} \tag{12}$$

where $\dot{\boldsymbol{\varepsilon}}^p$ is the unrotated plastic strain rate tensor, λ is the consistency parameter, and $\boldsymbol{M}$ is a unit tensor in the direction of the plastic strain rate. For associated plasticity, $\boldsymbol{M} = \hat{\boldsymbol{N}}$ where $\hat{\boldsymbol{N}}$ is the unit normal to the yield surface:

$$\dot{\boldsymbol{\varepsilon}}^p = \dot{\lambda}\hat{\boldsymbol{N}}\,, \quad \hat{\boldsymbol{N}} = \frac{\boldsymbol{N}}{\|\boldsymbol{N}\|}, \quad \boldsymbol{N} = \frac{\partial f}{\partial \boldsymbol{\sigma}} \tag{13}$$

where f is the yield function. Note that this normal cannot be determined from tabular data for states that lie outside the zero level set of the yield function. Therefore special consideration is needed. For non-associated plasticity, the direction of the plastic strain rate tensor is computed using

$$\dot{\boldsymbol{\varepsilon}}^p = \dot{\lambda}\boldsymbol{M}\,, \quad \boldsymbol{M} = \frac{\operatorname{dev}(\boldsymbol{N}) + \beta \operatorname{tr}(\boldsymbol{N})}{\|\operatorname{dev}(\boldsymbol{N}) + \beta \operatorname{tr}(\boldsymbol{N})\|} \tag{14}$$

where β is a parameter that can be adjusted to fit dilatation data, if available.

3.3 Coupled elastic-plastic response

While a continuous representation of elastic-plastic coupling is not essential for the modeling and simulation of the behavior of the test sand material, it is informative to examine the implications of that coupling on the governing equations (Brannon, 2007).

Inserting (6) and (5) into (4), we get

$$\dot{\boldsymbol{\sigma}} = \mathbf{C} : \dot{\boldsymbol{\varepsilon}}^e + \frac{\partial \boldsymbol{\sigma}}{\partial \varepsilon_v^p}\dot{\varepsilon}_v^p = 3K\dot{\boldsymbol{\varepsilon}}^e_{\text{iso}} + 2G\dot{\boldsymbol{\varepsilon}}^e_{\text{dev}} + \frac{\partial \boldsymbol{\sigma}}{\partial \varepsilon_v^p}\dot{\varepsilon}_v^p \tag{15}$$

where

$$\dot{\boldsymbol{\varepsilon}}^e_{\text{iso}} := \tfrac{1}{3}\operatorname{tr}(\dot{\boldsymbol{\varepsilon}}^e)\boldsymbol{I} \quad \text{and} \quad \dot{\boldsymbol{\varepsilon}}^e_{\text{dev}} := \dot{\boldsymbol{\varepsilon}}^e - \dot{\boldsymbol{\varepsilon}}^e_{\text{iso}}\,. \tag{16}$$

If we substitute (1) into (15), we get

$$\dot{\boldsymbol{\sigma}} = 3K(\dot{\boldsymbol{\varepsilon}}_{\text{iso}} - \dot{\boldsymbol{\varepsilon}}^p_{\text{iso}}) + 2G(\dot{\boldsymbol{\varepsilon}}_{\text{dev}} - \dot{\boldsymbol{\varepsilon}}^p_{\text{dev}}) + \frac{\partial \boldsymbol{\sigma}}{\partial \varepsilon_v^p}\dot{\varepsilon}_v^p \tag{17}$$

where $\dot{\boldsymbol{\varepsilon}}_{\text{iso}}$, $\dot{\boldsymbol{\varepsilon}}_{\text{dev}}$, $\dot{\boldsymbol{\varepsilon}}^p_{\text{iso}}$, and $\dot{\boldsymbol{\varepsilon}}^p_{\text{dev}}$ are defined analogously to the definitions in (16). Substitution of the flow rule (12) into (17) gives

$$\dot{\boldsymbol{\sigma}} = 3K(\dot{\boldsymbol{\varepsilon}}_{\text{iso}} - \dot{\lambda}\boldsymbol{M}_{\text{iso}}) + 2G(\dot{\boldsymbol{\varepsilon}}_{\text{dev}} - \dot{\lambda}\boldsymbol{M}_{\text{dev}}) + \frac{\partial \boldsymbol{\sigma}}{\partial \varepsilon_v^p}\dot{\varepsilon}_v^p \tag{18}$$

where

$$\boldsymbol{M}_{\text{iso}} := \tfrac{1}{3}\operatorname{tr}(\boldsymbol{M})\boldsymbol{I} \quad \text{and} \quad \boldsymbol{M}_{\text{dev}} := \boldsymbol{M} - \boldsymbol{M}_{\text{iso}}\,. \tag{19}$$

From the definition of the volumetric plastic strain rate (3) and using the flow rule (12), we have

$$\dot{\varepsilon}_v^p = \operatorname{tr}(\dot{\boldsymbol{\varepsilon}}^p) = \dot{\lambda}\operatorname{tr}(\boldsymbol{M})\,. \tag{20}$$

Therefore, equation (18) can be written as

$$\dot{\boldsymbol{\sigma}} = 3K(\dot{\boldsymbol{\varepsilon}}_{\text{iso}} - \dot{\lambda}\boldsymbol{M}_{\text{iso}}) + 2G(\dot{\boldsymbol{\varepsilon}}_{\text{dev}} - \dot{\lambda}\boldsymbol{M}_{\text{dev}}) + \dot{\lambda}\frac{\partial \boldsymbol{\sigma}}{\partial \varepsilon_v^p}\operatorname{tr}(\boldsymbol{M}) \tag{21}$$

Assuming all other quantities are known, we still need to determine the derivative of the stress with respect to the volumetric plastic strain and some assumptions are needed for us to be able to compute that. To determine the coupling term we use the approach suggested in Hueckel and Maier (1977) where we start with the nonlinear elastic model

$$\boldsymbol{\varepsilon}^e = \boldsymbol{\varepsilon}^e(\boldsymbol{\sigma}, \varepsilon_v^p) \tag{22}$$

The rate form of equation (22) is

$$\dot{\boldsymbol{\varepsilon}}^e = \frac{\partial \boldsymbol{\varepsilon}^e}{\partial \boldsymbol{\sigma}} : \dot{\boldsymbol{\sigma}} + \frac{\partial \boldsymbol{\varepsilon}^e}{\partial \varepsilon_v^p}\dot{\varepsilon}_v^p = \mathbf{S}(\boldsymbol{\sigma}, \varepsilon_v^p) : \dot{\boldsymbol{\sigma}} + \frac{\partial \boldsymbol{\varepsilon}^e}{\partial \varepsilon_v^p}\dot{\varepsilon}_v^p \tag{23}$$

where $\mathbf{S}(\boldsymbol{\sigma}, \varepsilon_v^p)$ is the rank-4 compliance tensor given by

$$\mathbf{S} = \mathbf{C}^{-1} = \tfrac{1}{3}\left(\frac{1}{3K(p, \varepsilon_v^p)} - \frac{1}{2G(p, \varepsilon_v^p)}\right)\boldsymbol{I} \otimes \boldsymbol{I} + \frac{1}{2G(p, \varepsilon_v^p)}\mathbf{I}\,, \quad p = \tfrac{1}{3}\mathrm{tr}(\boldsymbol{\sigma})\,. \tag{24}$$

We can contract $\mathbf{C}$ with (23) to get

$$\mathbf{C} : \dot{\boldsymbol{\varepsilon}}^e = \dot{\boldsymbol{\sigma}} + \left(\mathbf{C} : \frac{\partial \boldsymbol{\varepsilon}^e}{\partial \varepsilon_v^p}\right)\dot{\varepsilon}_v^p\,. \tag{25}$$

Comparing using (15) and (25), we have

$$\dot{\boldsymbol{\sigma}} = \mathbf{C} : \dot{\boldsymbol{\varepsilon}}^e - \left(\mathbf{C} : \frac{\partial \boldsymbol{\varepsilon}^e}{\partial \varepsilon_v^p}\right)\dot{\varepsilon}_v^p = \mathbf{C} : \dot{\boldsymbol{\varepsilon}}^e + \frac{\partial \boldsymbol{\sigma}}{\partial \varepsilon_v^p}\dot{\varepsilon}_v^p \quad \Longrightarrow \quad \frac{\partial \boldsymbol{\sigma}}{\partial \varepsilon_v^p} = -\mathbf{C} : \frac{\partial \boldsymbol{\varepsilon}^e}{\partial \varepsilon_v^p}\,. \tag{26}$$

An estimate for the partial derivative with respect to the plastic volumetric strain can be found by assuming that

$$\frac{\partial \boldsymbol{\varepsilon}^e}{\partial \varepsilon_v^p} \approx \frac{\partial \mathbf{S}}{\partial \varepsilon_v^p} : \boldsymbol{\sigma} = -\left[\frac{1}{3K^2}\frac{\partial K}{\partial \varepsilon_v^p}p\boldsymbol{I} + \frac{1}{2G^2}\frac{\partial G}{\partial \varepsilon_v^p}\boldsymbol{s}\right] \tag{27}$$

Then the derivative of stress with respect to the volumetric plastic strain can be expressed as

$$\frac{\partial \boldsymbol{\sigma}}{\partial \varepsilon_v^p} = \frac{1}{K}\frac{\partial K}{\partial \varepsilon_v^p}p\boldsymbol{I} + \frac{1}{G}\frac{\partial G}{\partial \varepsilon_v^p}\boldsymbol{s}\,. \tag{28}$$

We can now substitute (28) into (21) to get the elastic stress rate model that we seek:

$$\dot{\boldsymbol{\sigma}} = 3K(\dot{\boldsymbol{\varepsilon}}_{\mathrm{iso}} - \dot{\lambda}\boldsymbol{M}_{\mathrm{iso}}) + 2G(\dot{\boldsymbol{\varepsilon}}_{\mathrm{dev}} - \dot{\lambda}\boldsymbol{M}_{\mathrm{dev}}) + \dot{\lambda}\left[\frac{1}{K}\frac{\partial K}{\partial \varepsilon_v^p}p\boldsymbol{I} + \frac{1}{G}\frac{\partial G}{\partial \varepsilon_v^p}\boldsymbol{s}\right]\mathrm{tr}(\boldsymbol{M}) \tag{29}$$

Note that the above rate-form stress-strain relation has the general form

$$\dot{\boldsymbol{\sigma}} = \mathbf{C} : (\dot{\boldsymbol{\varepsilon}} - \dot{\lambda}\boldsymbol{M}) - \dot{\lambda}\boldsymbol{Z} \tag{30}$$

where $\boldsymbol{Z}$ is the elastic-plastic coupling term given by

$$\boldsymbol{Z} = -\left[\frac{1}{K}\frac{\partial K}{\partial \varepsilon_v^p}p\boldsymbol{I} + \frac{1}{G}\frac{\partial G}{\partial \varepsilon_v^p}\boldsymbol{s}\right]\mathrm{tr}(\boldsymbol{M})\,. \tag{31}$$

3.4 Trial stress and return projection operator

Since tabular data are available only for the zero level set of the yield function, standard return algorithms cannot be used for tabular elastoplasticity. Instead, an appropriate projection operation is needed to return the trial stress state to the yield surface. In this section we discuss the main features of such a projection operation.

For the plastic part of the loading process, the evolution of the compression cap requires that we assume that the stress state must lie on an evolving yield surface which is expressed as

$$f(\boldsymbol{\sigma}, \varepsilon_v^p) = 0\,. \tag{32}$$

The consistency condition requires that

$$\dot{\lambda}\dot{f} = 0\,. \tag{33}$$

During plastic loading, $\dot{\lambda} > 0$. Combining the time derivative of f with the flow rule (20), we have

$$\frac{\partial f}{\partial \boldsymbol{\sigma}} : \dot{\boldsymbol{\sigma}} = -\dot{\lambda}\frac{\partial f}{\partial \varepsilon_v^p}\mathrm{tr}(\boldsymbol{M})\,. \tag{34}$$

Noting that the derivative of f with respect to $\boldsymbol{\sigma}$ represents the normal to the yield surface in stress space, we can write

$$\hat{\boldsymbol{N}} : \dot{\boldsymbol{\sigma}} = \dot{\lambda} H \tag{35}$$

where $\hat{\boldsymbol{N}}$ is the unit normal to the yield surface, and H is a hardening modulus defined as

$$H := -\frac{\partial f}{\partial \varepsilon_v^p}\frac{\mathrm{tr}(\boldsymbol{M})}{\|\boldsymbol{N}\|}\,. \tag{36}$$

At this stage we can apply the standard projection of a trial stress state on to the yield surface. Let the rate of the trial stress be given by

$$\dot{\boldsymbol{\sigma}}^{\mathrm{trial}} = \mathbf{C} : \dot{\boldsymbol{\varepsilon}}\,. \tag{37}$$

Using (37) in (30) gives

$$\dot{\boldsymbol{\sigma}} = \dot{\boldsymbol{\sigma}}^{\mathrm{trial}} - \dot{\lambda}(\mathbf{C} : \boldsymbol{M} + \boldsymbol{Z}) = \dot{\boldsymbol{\sigma}}^{\mathrm{trial}} - \dot{\lambda}\boldsymbol{P} \tag{38}$$

where

$$\boldsymbol{P} := \mathbf{C} : \boldsymbol{M} + \boldsymbol{Z}\,. \tag{39}$$

From (35) and (38), solving for $\dot{\lambda}$, we get

$$\dot{\lambda} = \frac{\hat{\boldsymbol{N}} : \dot{\boldsymbol{\sigma}}^{\mathrm{trial}}}{\hat{\boldsymbol{N}} : \boldsymbol{P} + H}\,. \tag{40}$$

Substituting (40) in (38), we have

$$\dot{\boldsymbol{\sigma}} = \mathbf{H} : \dot{\boldsymbol{\sigma}}^{\mathrm{trial}}\,, \quad \mathbf{H} := \mathbf{I} - \frac{\boldsymbol{P} \otimes \hat{\boldsymbol{N}}}{\boldsymbol{P} : \hat{\boldsymbol{N}} + H}\,. \tag{41}$$

Let us define a linear projection operator, $\mathbf{P}$, such that (Brannon, 2007)

$$\mathbf{P} := \mathbf{I} - \frac{\boldsymbol{P} \otimes \hat{\boldsymbol{N}}}{\boldsymbol{P} : \hat{\boldsymbol{N}}}\,. \tag{42}$$

Then

$$\mathbf{P} : \boldsymbol{A} = \mathbf{P} : \boldsymbol{B} \quad \text{iff} \quad \boldsymbol{A} = \boldsymbol{B} + \alpha \boldsymbol{P} \tag{43}$$

where α is a scalar, and

$$\mathbf{H} = \mathbf{P} - \left(\frac{1}{\boldsymbol{P} : \hat{\boldsymbol{N}} + H} - \frac{1}{\boldsymbol{P} : \hat{\boldsymbol{N}}} \right) \boldsymbol{P} \otimes \hat{\boldsymbol{N}} \,. \tag{44}$$

We use the above relation between $\mathbf{H}$ and $\mathbf{P}$ to show that

$$\mathbf{P} : (\mathbf{H} : \boldsymbol{A}) = \mathbf{P} : \boldsymbol{A} \tag{45}$$

for any rank-2 tensor $\boldsymbol{A}$, which implies that $\mathbf{H} : \dot{\boldsymbol{\sigma}}^{\text{trial}}$ can be expressed as a linear combination of $\dot{\boldsymbol{\sigma}}^{\text{trial}}$ and $\boldsymbol{P}$. This observation will be useful for designing a closest point return algorithm in the appropriate transformed stress space.

4 Stress update

Equation (41) is continuous and the projection operator $\mathbf{H}$ requires that we know the stress state ($\boldsymbol{\sigma}$) at every instant of time before it can be evaluated. For materials where $\mathbf{C}$ is a function of the elastic and plastic strains, even the determination of the trial stress requires that we know the final stress. Since the final stress state is unknown and typically cannot be solved in closed-form, a discretized "stress-update" algorithm is required that can provide an approximate stress. This is achieved by approximately integrating (41) over a (small) timestep Δt.

Let the known values at the beginning of the timestep (t_n) be $\boldsymbol{\sigma}_n$, $\boldsymbol{\varepsilon}_n$, $(\varepsilon_v^e)_n$, $(\varepsilon_v^p)_n$, $\mathbf{C}_n$, K_n, and G_n. Let those at the end of the timestep (t_{n+1}) be $\boldsymbol{\sigma}_{n+1}$, $\boldsymbol{\varepsilon}_{n+1}$, $(\varepsilon_v^e)_{n+1}$, $(\varepsilon_v^p)_{n+1}$, $\mathbf{C}_{n+1}$, K_{n+1}, and G_{n+1}. In a strain-driven calculation, we know $\boldsymbol{\varepsilon}_{n+1}$ but the rest of the quantities at t_{n+1} are unknown. If a first-order finite difference scheme and a small timestep ($\Delta t = t_{n+1} - t_n$) is used, we have

$$\dot{\boldsymbol{\sigma}} = \frac{\boldsymbol{\sigma}_{n+1} - \boldsymbol{\sigma}_n}{\Delta t} \quad \text{and} \quad \dot{\boldsymbol{\sigma}}^{\text{trial}} = \frac{\boldsymbol{\sigma}_{n+1}^{\text{trial}} - \boldsymbol{\sigma}_n}{\Delta t} = \frac{\mathbf{C}_n : (\boldsymbol{\varepsilon}_{n+1} - \boldsymbol{\varepsilon}_n)}{\Delta t} \,. \tag{46}$$

For elastic-plastic deformations, equation (41) applies for the part of the timestep that is plastic, i.e., $\dot{\lambda} = 0$. Let Δt_e be the elastic part, if any, of the timestep. Then,

$$\dot{\boldsymbol{\sigma}}_e = \dot{\boldsymbol{\sigma}}^{\text{trial}} = \frac{\boldsymbol{\sigma}_e^{\text{trial}} - \boldsymbol{\sigma}_n}{\Delta t_e} = \frac{\mathbf{C}_n : (\boldsymbol{\varepsilon}_{n+1}^e - \boldsymbol{\varepsilon}_n)}{\Delta t_e} \,. \tag{47}$$

where $\boldsymbol{\sigma}_e^{\text{trial}}$ is stress at the end of the elastic interval and $\boldsymbol{\varepsilon}_{n+1}^e$ is the elastic strain at the end of the time increment. For the plastic part of the timestep, $\Delta t_p = \Delta t - \Delta t_e$, we have

$$\dot{\boldsymbol{\sigma}}_p = \mathbf{H} : \dot{\boldsymbol{\sigma}}^{\text{trial}} = \frac{\boldsymbol{\sigma}_{n+1} - \boldsymbol{\sigma}_e^{\text{trial}}}{\Delta t_p} \tag{48}$$

Combining (47) and (48),

$$\boldsymbol{\sigma}_{n+1} = \boldsymbol{\sigma}_n + \mathbf{H} : \dot{\boldsymbol{\sigma}}^{\text{trial}} \Delta t_p + \dot{\boldsymbol{\sigma}}^{\text{trial}} \Delta t_e \,. \tag{49}$$

Substituting for $\boldsymbol{\sigma}_n$ with the second of equations (46), we have

$$\boldsymbol{\sigma}_{n+1} = \boldsymbol{\sigma}_{n+1}^{\text{trial}} + \mathbf{H} : \dot{\boldsymbol{\sigma}}^{\text{trial}} \Delta t_p - \dot{\boldsymbol{\sigma}}^{\text{trial}} \Delta t_p \,. \tag{50}$$

Let us now apply the projection $\mathbf{P}$ to equation (50). Then

$$\mathbf{P} : \boldsymbol{\sigma}_{n+1} = \mathbf{P} : \boldsymbol{\sigma}_{n+1}^{\text{trial}} + \mathbf{P} : \mathbf{H} : \dot{\boldsymbol{\sigma}}^{\text{trial}} \Delta t_p - \mathbf{P} : \dot{\boldsymbol{\sigma}}^{\text{trial}} \Delta t_p \,. \tag{51}$$

Using (45) we get

$$\mathbf{P} : \boldsymbol{\sigma}_{n+1} = \mathbf{P} : \boldsymbol{\sigma}_{n+1}^{\text{trial}} + \mathbf{P} : \dot{\boldsymbol{\sigma}}^{\text{trial}} \Delta t_p - \mathbf{P} : \dot{\boldsymbol{\sigma}}^{\text{trial}} \Delta t_p = \mathbf{P} : \boldsymbol{\sigma}_{n+1}^{\text{trial}} \,. \tag{52}$$

From (43) and (52), we see that

$$\boldsymbol{\sigma}_{n+1} = \boldsymbol{\sigma}_{n+1}^{\text{trial}} + \alpha \boldsymbol{P}_{n+1} \tag{53}$$

where α is a scalar and

$$\begin{aligned} \boldsymbol{P}_{n+1} &= \mathbf{C}_{n+1} : \boldsymbol{M}_{n+1} + \boldsymbol{Z}_{n+1} \\ \boldsymbol{Z}_{n+1} &= -\left[\frac{1}{K_{n+1}} \frac{\partial K}{\partial \varepsilon_v^p} \bigg|_{n+1} p_{n+1} \boldsymbol{I} + \frac{1}{G_{n+1}} \frac{\partial G}{\partial \varepsilon_v^p} \bigg|_{n+1} \boldsymbol{s}_{n+1} \right] \text{tr}(\boldsymbol{M}_{n+1}) \,. \end{aligned} \tag{54}$$

Comparison of (53) with (38) indicates that

$$\alpha = -(\lambda_{n+1} - \lambda_n) = -\Delta\lambda =: -\Gamma \,. \tag{55}$$

Therefore we can write

$$\boldsymbol{\sigma}_{n+1} = \boldsymbol{\sigma}_{n+1}^{\text{trial}} - \Gamma \boldsymbol{P}_{n+1} \quad \text{where} \quad \Gamma = \dot{\lambda} \Delta t_p \,. \tag{56}$$

Even though the plastic part of the time step is not necessary to solve this stress update equation, it still requires an iterative approach if the unknown quantities at t_{n+1} are to be determined.

4.1 Closest point projection

The first step in the iterative approach is to compute a closest point projection of a trial stress to the yield surface. To compute the trial stress, we assume that the stiffness matrix is constant such that $\boldsymbol{\sigma}^{\text{trial}} = \boldsymbol{\sigma}_n + \mathbf{C}_n : (\boldsymbol{\varepsilon}_{n+1} - \boldsymbol{\varepsilon}_n)$. We also assume that the yield surface is fixed and normals to the surface do not change over the timestep. Let $g(\boldsymbol{\sigma}^{\text{trial}})$ be the value of the yield function at the trial state. Let $\boldsymbol{\sigma}_{n+1}$ be actual stress under these assumptions and let $g(\boldsymbol{\sigma}_{n+1}) = 0$ be the value of the yield function at the actual stress state.

If we assume the actual stress state on the yield surface is at the closest distance from the trial stress, we can devise the primal minimization problem:

$$\begin{aligned} &\text{minimize} \quad f(\boldsymbol{\sigma}) = \| \boldsymbol{\sigma}^{\text{trial}} - \boldsymbol{\sigma} \|^2 \,, \quad \| \boldsymbol{\sigma} \| := \sqrt{\boldsymbol{\sigma} : \boldsymbol{\sigma}} \\ &\text{subject to} \quad g(\boldsymbol{\sigma}) \leq 0 \end{aligned} \tag{57}$$

The Lagrangian for this problem is

$$\mathcal{L}(\boldsymbol{\sigma}, \lambda) = f(\boldsymbol{\sigma}) + \Delta\lambda g(\boldsymbol{\sigma}) = \| \boldsymbol{\sigma}^{\text{trial}} - \boldsymbol{\sigma} \|^2 + \Delta\lambda g(\boldsymbol{\sigma}) \tag{58}$$

The Karush-Kuhn-Tucker conditions for this problem at the optimum value $\boldsymbol{\sigma}_{n+1}$ are

$$g(\boldsymbol{\sigma}_{n+1}) \leq 0 \,, \quad \Delta\lambda \geq 0 \,, \quad \Delta\lambda g(\boldsymbol{\sigma}_{n+1}) = 0 \,, \quad \frac{\partial f(\boldsymbol{\sigma}_{n+1})}{\partial \boldsymbol{\sigma}} + \Delta\lambda \frac{\partial g(\boldsymbol{\sigma}_{n+1})}{\partial \boldsymbol{\sigma}} = 0 \,. \tag{59}$$

From the last condition we see that the closest distance using this criterion leads to a stress value of

$$\boldsymbol{\sigma}_{n+1} = \boldsymbol{\sigma}^{\text{trial}} - \tfrac{1}{2}\Delta\lambda \frac{\partial g(\boldsymbol{\sigma}_{n+1})}{\partial \boldsymbol{\sigma}} \tag{60}$$

But we have seen previously in equation (56) that the first-order stress update leads to

$$\boldsymbol{\sigma}_{n+1} = \boldsymbol{\sigma}^{\text{trial}} - \Gamma \boldsymbol{P}_{n+1} = \boldsymbol{\sigma}^{\text{trial}} - \Delta\lambda(\mathbf{C}_{n+1} : \boldsymbol{M}_{n+1} + \boldsymbol{Z}_{n+1}) \,. \tag{61}$$

For associated plasticity $\boldsymbol{M}_{n+1} = \hat{\boldsymbol{N}}_{n+1} = \partial g_{n+1}/\partial \boldsymbol{\sigma}$, and with the assumption that $\mathbf{C}$ is fixed, $\mathbf{C}_{n+1} = \mathbf{C}_n$ and $\boldsymbol{Z}_{n+1} = \mathbf{0}$. Incorporating the normalizing factor for the yield surface normals into λ, we have

$$\boldsymbol{\sigma}_{n+1} = \boldsymbol{\sigma}^{\text{trial}} - \Delta\lambda \mathbf{C}_n : \frac{\partial g(\boldsymbol{\sigma}_{n+1})}{\partial \boldsymbol{\sigma}} \,. \tag{62}$$

The similarity between the (60) and (62) indicates that the actual stress state is at a "closest" point from the trial stress state. However, the correct closest distance is not in the standard standard stress space, but in a space where the norm to be minimized is given by (Simo and Hughes, 2006)

$$\|\boldsymbol{\sigma}\|_{\mathbf{C}^{-1}} = \sqrt{\boldsymbol{\sigma} : \mathbf{C}^{-1} : \boldsymbol{\sigma}} = \sqrt{\boldsymbol{\sigma} : \mathbf{S} : \boldsymbol{\sigma}} = \|\boldsymbol{\sigma}\|_{\mathbf{S}} \,. \tag{63}$$

This can be verified by computing the optimality conditions for a minimization problem with the modified norm.

The distance measure

$$\|\boldsymbol{\sigma}\|_{\mathbf{S}} = \sqrt{\boldsymbol{\sigma} : \mathbf{S} : \boldsymbol{\sigma}} \tag{64}$$

can be interpreted as a standard Euclidean distance measure in a transformed stress space by observing that (Homel, 2015)

$$\|\boldsymbol{\sigma}\|_{\mathbf{S}} = \sqrt{(\boldsymbol{\sigma} : \mathbf{S}^{1/2}) : (\mathbf{S}^{1/2} : \boldsymbol{\sigma})} = \sqrt{(\mathbf{S}^{1/2} : \boldsymbol{\sigma}) : (\mathbf{S}^{1/2} : \boldsymbol{\sigma})} = \sqrt{\boldsymbol{\sigma}^\star : \boldsymbol{\sigma}^\star} = \|\boldsymbol{\sigma}^\star\|_2 \tag{65}$$

where we have used the major symmetry of $\mathbf{S} = \mathbf{S}^{1/2} : \mathbf{S}^{1/2}$.

Note that this particular closest-point interpretation applies only for perfect plasticity and only associative flow rules. For hardening plasticity, the space in which the actual stress is closest to the trial stress is different. For non-associative plasticity, it is unclear whether any closest-point approach can be rigorously justified.

The transformed stress tensor can expressed as (Homel, 2015)

$$\boldsymbol{\sigma}^\star = \mathbf{S}^{1/2} : \boldsymbol{\sigma} = \left[\frac{1}{\sqrt{3\kappa}} \mathbf{P}^{\text{iso}} + \frac{1}{\sqrt{2\mu}} \mathbf{P}^{\text{symdev}} \right] : (z\,\mathbf{E}_z + r\,\mathbf{E}_r) \,. \tag{66}$$

where

$$\mathbf{P}^{\text{iso}} = \tfrac{1}{3} \boldsymbol{I} \otimes \boldsymbol{I} \,, \quad \mathbf{P}^{\text{symdev}} = \mathbf{I} - \mathbf{P}^{\text{iso}} \tag{67}$$

and the stress tensor has been expressed in the Lode basis (Brannon, 2007)

$$\boldsymbol{\sigma} = z\,\boldsymbol{E}_z + r\,\boldsymbol{E}_r \,, \quad z = \tfrac{1}{\sqrt{3}} \operatorname{tr}(\boldsymbol{\sigma}) \,, \quad r = \|\boldsymbol{s}\|_2 \,, \quad \boldsymbol{E}_z = \tfrac{1}{\sqrt{3}} \boldsymbol{I} \,, \quad \boldsymbol{E}_r = \frac{\boldsymbol{s}}{\|\boldsymbol{s}\|_2} \,. \tag{68}$$

We can show that

$$\mathbf{P}^{\text{iso}} : \boldsymbol{E}_z = \boldsymbol{E}_z \,, \quad \mathbf{P}^{\text{iso}} : \boldsymbol{E}_r = \boldsymbol{0} \,, \quad \mathbf{P}^{\text{symdev}} : \boldsymbol{E}_z = \boldsymbol{0} \,, \quad \mathbf{P}^{\text{symdev}} : \boldsymbol{E}_r = \boldsymbol{E}_r \,. \tag{69}$$

Therefore,

$$\boldsymbol{\sigma}^\star = \frac{z}{\sqrt{3\kappa}} \mathbf{E}_z + \frac{r}{\sqrt{2\mu}} \mathbf{E}_r \,. \tag{70}$$

The transformed stress remains geometrically unchanged (angles do not change) if we express it as

$$\boldsymbol{\sigma}^\star = z \, \mathbf{E}_z + \sqrt{\frac{3\kappa}{2\mu}} \, r \, \mathbf{E}_r =: z \, \mathbf{E}_z + r' \, \mathbf{E}_r \,. \tag{71}$$

This straightforward way of computing stresses in the transformed space can be used directly in a geometrical closest point projection algorithm.

4.2 Iterative solution

We can now apply a multi-stage return algorithm (Brannon and Leelavanichkul, 2010) to determine the updated state. The trial stress is computed using $\boldsymbol{\sigma}^{\text{trial}}_{n+1} = \boldsymbol{\sigma}_n + \mathbf{C}_n : (\boldsymbol{\varepsilon}_{n+1} - \boldsymbol{\varepsilon}_n)$. The algorithm has four stages:

1. Keeping all quantities fixed at the beginning of the timestep, use a geometric closest point return algorithm to determine an estimate of $\boldsymbol{\sigma}_{n+1}$. Let us call this estimate $\boldsymbol{\sigma}^C_{n+1}$ with the superscript C indicating that this is the geometric closest point.
2. Still keeping all quantities fixed, compute an improved estimate for $\boldsymbol{\sigma}_{n+1}$. Let us denote this estimate as $\boldsymbol{\sigma}^F_{n+1}$ with the superscript F indicating that the elastic moduli and internal variables have been kept fixed. The elastic and plastic strains for this state are $(\boldsymbol{\varepsilon}^e_{n+1})^F$ and $(\boldsymbol{\varepsilon}^p_{n+1})^F$, and their volumetric components are $(\varepsilon^e_v)^F$ and $(\varepsilon^p_v)^F$, respectively.
3. In the third step we find estimates of $\boldsymbol{\sigma}_{n+1} = \boldsymbol{\sigma}^H_{n+1}$, $\boldsymbol{\varepsilon}^e_{n+1} = (\boldsymbol{\varepsilon}^e_{n+1})^H$ and $\boldsymbol{\varepsilon}^p_{n+1} = (\boldsymbol{\varepsilon}^p_{n+1})^H$ while varying the internal variables. The superscript H indicates that during this stage hardening is included in the algorithm.
4. In the final step, a closest point projection is used to move $\boldsymbol{\sigma}^H_{n+1}$ back to the yield surface to the point $\boldsymbol{\sigma}_{n+1}$. The elastic and plastic strains, $\boldsymbol{\varepsilon}^e_{n+1}$ and $\boldsymbol{\varepsilon}^p_{n+1}$, are computed and used to update the elastic moduli. This procedure implicitly assumes that elastic moduli vary in a stepped manner and therefore requires that time increments be small.

Assume that we have an estimate for $\boldsymbol{\sigma}^C_{n+1}$. Then we can write,

$$\boldsymbol{\sigma}^F_{n+1} - \boldsymbol{\sigma}^{\text{trial}}_{n+1} = (\boldsymbol{\sigma}^F_{n+1} - \boldsymbol{\sigma}^C_{n+1}) + (\boldsymbol{\sigma}^C_{n+1} - \boldsymbol{\sigma}^{\text{trial}}_{n+1}) \tag{72}$$

Let the yield function unit normal evaluated at the closest-point stress estimate be

$$\hat{\boldsymbol{N}}^C = \frac{\boldsymbol{N}^C}{\|\boldsymbol{N}^C\|} \,, \quad \boldsymbol{N}^C = \frac{\partial}{\partial \boldsymbol{\sigma}} [f(\boldsymbol{\sigma}, \varepsilon^p_v)] \Big|_{\boldsymbol{\sigma}=\boldsymbol{\sigma}^C_{n+1}, \varepsilon^p_v = (\varepsilon^p_v)_n} \,. \tag{73}$$

Then

$$(\boldsymbol{\sigma}^F_{n+1} - \boldsymbol{\sigma}^{\text{trial}}_{n+1}) : \hat{\boldsymbol{N}}^C = (\boldsymbol{\sigma}^F_{n+1} - \boldsymbol{\sigma}^C_{n+1}) : \hat{\boldsymbol{N}}^C + (\boldsymbol{\sigma}^C_{n+1} - \boldsymbol{\sigma}^{\text{trial}}_{n+1}) : \hat{\boldsymbol{N}}^C \tag{74}$$

When the states $\boldsymbol{\sigma}^F_{n+1}$ and $\boldsymbol{\sigma}^C_{n+1}$ are close to each other (or when the curvature of the yield surface between these points is relatively small), we can make the assumption that

$$(\boldsymbol{\sigma}^F_{n+1} - \boldsymbol{\sigma}^C_{n+1}) : \hat{\boldsymbol{N}}^C \approx 0 \,. \tag{75}$$

Also, for a fixed yield surface, with $\Gamma^F := \lambda^F_{n+1} - \lambda_n$,

$$\boldsymbol{\sigma}^F_{n+1} - \boldsymbol{\sigma}^{\text{trial}}_{n+1} = -\Gamma^F \boldsymbol{P}_n \,. \tag{76}$$

Substituting (75) and (76) into (74) we have

$$\Gamma^F \approx -\frac{(\boldsymbol{\sigma}^C_{n+1} - \boldsymbol{\sigma}^{\text{trial}}_{n+1}) : \hat{\boldsymbol{N}}^C}{\boldsymbol{P}_n : \hat{\boldsymbol{N}}^C} \,. \tag{77}$$

The improved stress estimate, $\boldsymbol{\sigma}^F_{n+1}$, is obtained by substituting (77) into (76):

$$\boldsymbol{\sigma}^F_{n+1} \approx \boldsymbol{\sigma}^{\text{trial}}_{n+1} + \frac{(\boldsymbol{\sigma}^C_{n+1} - \boldsymbol{\sigma}^{\text{trial}}_{n+1}) : \hat{\boldsymbol{N}}^C}{\boldsymbol{P}_n : \hat{\boldsymbol{N}}^C} \boldsymbol{P}_n \,. \tag{78}$$

The updated unit normal to the yield surface is

$$\hat{\boldsymbol{N}}^F = \frac{\boldsymbol{N}^F}{\|\boldsymbol{N}^F\|} \,, \quad \boldsymbol{N}^F = \frac{\partial}{\partial \boldsymbol{\sigma}} [f(\boldsymbol{\sigma}, \varepsilon^p_v)] \Big|_{\boldsymbol{\sigma} = \boldsymbol{\sigma}^F_{n+1}, \varepsilon^p_v = (\varepsilon^p_v)_n} \,. \tag{79}$$

The stress state $\boldsymbol{\sigma}^F_{n+1}$ likely does not lie on the yield surface, and an iterative method is required to make sure it is close to the yield surface as shown in the following pseudo-code.

Algorithm 1 Computing $\boldsymbol{\sigma}^F_{n+1}$, $\hat{\boldsymbol{N}}^F$, $\boldsymbol{P}^F$, H^F, and Γ^F iteratively.

Require: $\boldsymbol{\sigma}_n$, $\mathbf{C}_n$, $\boldsymbol{Z}_n$, $\boldsymbol{N}_n$, $\boldsymbol{M}_n$, $\boldsymbol{\sigma}^{\text{trial}}_{n+1}$

procedure COMPUTESIGMAF
  $k \leftarrow 0$, $\Gamma^F_k \leftarrow 0$, $\boldsymbol{\sigma}^F_{n+1,k} \leftarrow \boldsymbol{\sigma}^{\text{trial}}_{n+1}$.
  repeat
    Compute $\boldsymbol{\sigma}^C_{n+1,k+1}$ using closest point return to yield surface of $\boldsymbol{\sigma}^F_{n+1,k}$.
    Compute $\boldsymbol{N}^C_{n+1,k+1}$ using (73).
    Compute $\boldsymbol{M}^C_{n+1,k+1}$ using (14).
    Update $\boldsymbol{P}_{n,k+1} = \mathbf{C}_n : \boldsymbol{M}^C_{n+1,k+1} + \boldsymbol{Z}_n$.
    Compute Γ^F_{k+1} using (77)
    Compute $\boldsymbol{\sigma}^F_{n+1,k+1} \leftarrow \boldsymbol{\sigma}^{\text{trial}}_{n+1} - \Gamma^F_{k+1} \boldsymbol{P}_{n,k+1}$
    Update $k \leftarrow k + 1$
  until $(\Gamma^F_{k+1} - \Gamma^F_k) < \epsilon$
  Update $\boldsymbol{\sigma}^F_{n+1} \leftarrow \boldsymbol{\sigma}^F_{n+1,k+1}$, $\boldsymbol{P}^F \leftarrow \boldsymbol{P}_{n,k+1}$, and $\Gamma^F \leftarrow \Gamma^F_{k+1}$
  Update $\hat{\boldsymbol{N}}^F$, $\boldsymbol{N}^F$, $\boldsymbol{M}^F$ using (79).
  Compute $H^F = -\left(\dfrac{\partial f}{\partial \varepsilon^p_v} \Big|_{\boldsymbol{\sigma} = \boldsymbol{\sigma}^F_{n+1}, \varepsilon^p_v = (\varepsilon^p_v)_n} \right) \dfrac{\text{tr}(\boldsymbol{M}^F)}{\|\boldsymbol{N}^F\|}$.
  return $\boldsymbol{\sigma}^F_{n+1}$, $\boldsymbol{P}^F$, $\hat{\boldsymbol{N}}^F$, H^F, and Γ^F

16: **end procedure**

In the third stage of the process, we have to consider changes to the yield surface due to the evolution of internal variables. From the consistency condition (35), a first order approximation of the displacement of the yield surface (along the yield surface normal) during the time increment Δt is (using (55))

$$\hat{\boldsymbol{N}} : (\boldsymbol{\sigma}_{n+1} - \boldsymbol{\sigma}_n) = (\lambda_{n+1} - \lambda_n) H = \Gamma H \,. \tag{80}$$

We implicitly assume that the normal to the yield surface does not change during the timestep. This observation indicates that we can update the value of Γ for hardening/softening plasticity using the approximation (Brannon, 2007)

$$\Gamma^H = \Gamma^F \frac{\boldsymbol{P}^F : \hat{\boldsymbol{N}}^F}{\boldsymbol{P}^F : \hat{\boldsymbol{N}}^F + H^F} \tag{81}$$

After Γ^H has been found, we can compute $\boldsymbol{\sigma}^H_{n+1}$ using

$$\boldsymbol{\sigma}^H_{n+1} = \boldsymbol{\sigma}^{\text{trial}}_{n+1} - \Gamma^H \boldsymbol{P}^F \,. \tag{82}$$

This stress state may not lie on the yield surface, and a closest point projection is needed to force it back to the yield surface. This is the final stress state, $\boldsymbol{\sigma}_{n+1}$.

The corresponding increment in elastic strain can be computed using

$$\Delta(\boldsymbol{\varepsilon}^e_{n+1}) = (\boldsymbol{\varepsilon}^e_{n+1}) - \boldsymbol{\varepsilon}^e_n = \mathbf{C}^{-1}_n : (\boldsymbol{\sigma}_{n+1} - \boldsymbol{\sigma}_n) \,. \tag{83}$$

The incremental plastic strain can then be computed using

$$\Delta(\boldsymbol{\varepsilon}^p_{n+1}) = (\boldsymbol{\varepsilon}^p_{n+1}) - \boldsymbol{\varepsilon}^p_n = (\boldsymbol{\varepsilon}_{n+1} - \boldsymbol{\varepsilon}_n) - \Delta(\boldsymbol{\varepsilon}^e_{n+1}) \,. \tag{84}$$

Volumetric components of these strains can then be computed by taking the trace of these increments and adding them to the accumulated values. These are then used to update the elastic moduli in preparation for the next timestep.

5 Special considerations for tabular data

During the stress update process, a trial stress state is computed using the discretized trial stress rate in (46). This computation requires the elastic moduli, $\mathbf{C}$, to be extracted from the tabular data as described in previous work (Banerjee, Fox, and Regueiro, 2020a). The elastic moduli table can also be used to compute the derivatives needed in the elastic-plastic coupling term, $\boldsymbol{Z}$. Since a return algorithm is used, the stress state is available before the elastic strain. Therefore, computation more convenient if we use a table of bulk moduli as a function of pressure (mean stress) as depicted in Figure 5. As can be seen in the figure, the experimental data are not smooth and improved interpolations of the data can be performed if the input tables are smoothed prior to use in simulations.

After the trial stress state has been computed, a check is needed to determine whether this state in inside or outside the yield surface. To ensure convexity of yield surface, a convex hull of the tabular data representing $g(p)$ should be computed (see Figure 6) and points that do not fall on the hull should be removed from the table.

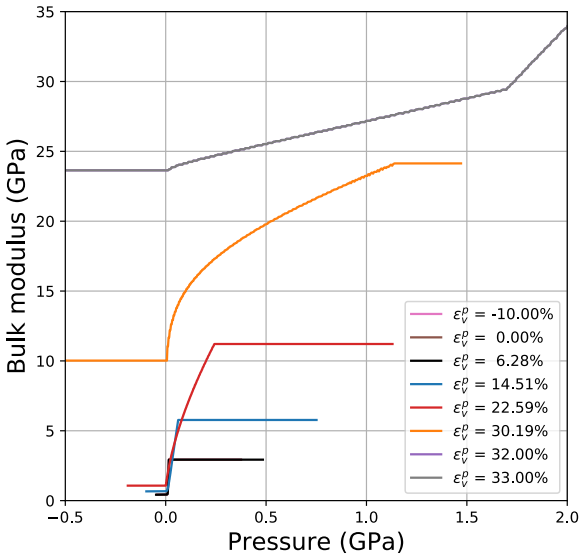

Figure 5 – *Bulk modulus table expressed as a function of pressure.*

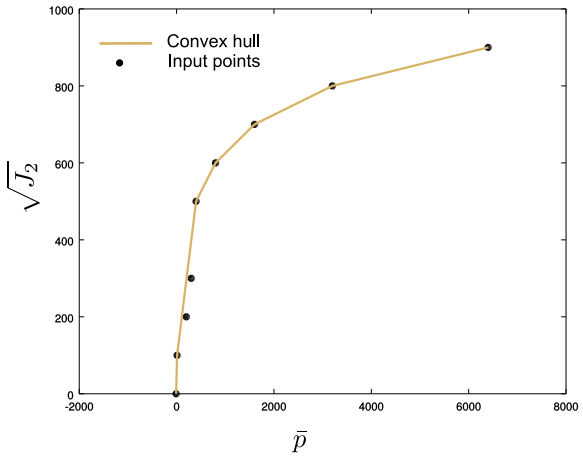

Figure 6 – *The function $g(\bar{p})$ corrected using a convex hull. The notation $\bar{p}$ is used to facilitate comparisons with previous work. Note that $\bar{p} = -p$ when the convention is that tension is positive.*

Since the yield surface consists of a table for $g(p)$ and a continuous function for $F_c(p)$ (see equation (9)), a preliminary check for the whether a stress state is plastic can be performed by comparing it with the rectangle bounding the yield function. A secondary test, applicable when $p \leq \kappa$ is to use linear interpolation to find the value of the yield function, $g(p)$, at a given value of p and compare the trial value of $\sqrt{J_2}$ at that state. A direct evaluation of the yield function is possible for $p > \kappa$.

However, the composite yield function used in this process contains numerous vertices where the normal to the yield surface is not well-defined. If these vertices are to be avoided, the straightforward checks in the previous paragraph are not sufficient. A more elaborate approach is needed to determine the value of $f(p, \sqrt{J_2})$ and $\partial f / \partial \boldsymbol{\sigma}$.

First, $F_c(p)$ is discretized and appended to the table for $g(p)$ (which is truncated or extended by linear extrapolation as required) as shown in Figure 7. The number of points, $(p, \sqrt{J_2})$, in the composite discretized yield function can be large (of the order of $> 10^3$). To facilitate searches, we can create a kd-tree (Blanco and Rai, 2014) from the point set. The closest segments on the yield surface from a given trial stress can then be computed using a nearest neighbor search of the kd-tree. The three points corresponding to the two closest segments can then be used to fit a open, uniform, quadratic B-spline. A Newton method, as described below, can then be used to find the closest point on the spline from the trial stress.

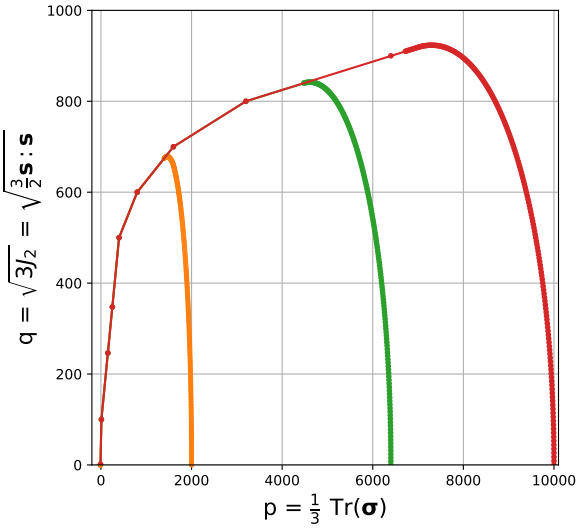

Figure 7 – *The cap function $F_c(p)$ is discretized and joined to a truncated or extended table of values of $g(p)$ to form the composite yield function.*

Let $\mathbf{p}_0$, $\mathbf{p}_1$ and $\mathbf{p}_2$ be the three control points of the quadratic B-spline. In matrix form, the parametric equation of the spline, $\mathbf{b}(t)$ is (Gordon and Riesenfeld, 1974)

$$\begin{bmatrix} b_x & b_y \end{bmatrix} = \begin{bmatrix} 1 & t & t^2 \end{bmatrix} [\mathrm{S}] \begin{bmatrix} p_{0x} & p_{0y} \\ p_{1x} & p_{1y} \\ p_{2x} & p_{2y} \end{bmatrix} \tag{85}$$

where the spline matrix $[\mathsf{S}]$ is one of

$$[\mathsf{S}]_0 = \begin{bmatrix} 2 & 0 & 0 \\ -4 & 4 & 0 \\ 2 & -3 & 1 \end{bmatrix}, \quad [\mathsf{S}]_1 = \begin{bmatrix} 1 & 1 & 0 \\ -2 & 2 & 0 \\ 1 & -2 & 1 \end{bmatrix}, \quad [\mathsf{S}]_2 = \begin{bmatrix} 1 & 1 & 0 \\ -2 & 2 & 0 \\ 1 & -3 & 2 \end{bmatrix}. \tag{86}$$

The matrix $[\mathsf{S}]_0$ is used if the closest segments include the starting point of the yield function, $[\mathsf{S}]_2$ if the segments include the last point, and $[\mathsf{S}]_1$ is used for all other segments. The closest point $\mathbf{p}^c$ from a point $\mathbf{p}^{\text{trial}}$ to the spline $\mathbf{b}$ is the zero of the function

$$\chi(t) = [\mathbf{p}^{\text{trial}} - \mathbf{b}(t)] \cdot \frac{d\mathbf{b}}{dt}. \tag{87}$$

The Jacobian of this function is

$$\frac{d\chi}{dt} = -\frac{d\mathbf{b}}{dt} \cdot \frac{d\mathbf{b}}{dt} + [\mathbf{p}^{\text{trial}} - \mathbf{b}(t)] \cdot \frac{d^2\mathbf{b}}{dt^2}. \tag{88}$$

Newton's method for finding the value of t at which $\chi = 0$ can then be expressed as

$$t_{k+1} = t_k - \left[\frac{d\chi}{dt}\right]_k^{-1} \chi(t_k) \tag{89}$$

Upon termination of the iterative process, the closest point on the spline is computed using $\mathbf{p}^c = \mathbf{b}(t^{k+1})$ and the tangent at that point is $\mathbf{t}^c = d\mathbf{b}/dt|_{k+1}$. A schematic of the closest point computation process is depicted in Figure 8.

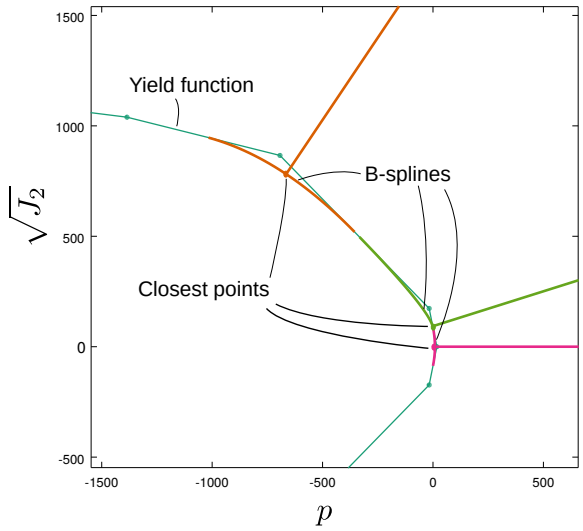

Figure 8 – *The closest point is computed to a smooth B-spline based approximation to the yield function. This process becomes more accurate as the number of points representing the yield function increases.*

The closest point computed with this process represents the actual location of the smoothed yield surface, and trial stress states determined to be elastic using the simple checks discussed earlier may

no longer be elastic with respect to the actual yield surface. However, whether the trial stress is inside or outside the spline can be determined by examining the sign of the implicit function $B(x, y)$ that corresponds to the parameterized curve $\mathbf{b}(t)$. An easier alternative is to find the orientation of the polygon ($\mathbf{p}_0$, $\mathbf{p}^c$, $\mathbf{p}_1$, $\mathbf{p}^{\text{trial}}$) using the Shoelace formula (Feito, Torres, and Urena, 1995)

$$Q = (p_x^c - p_{0x})(p_y^c + p_{0y}) + (p_{1x} - p_x^c)(p_{1y} + p_y^c) + (p_x^{\text{trial}} - p_{1x})(p_y^{\text{trial}} + p_{1y}) + (p_{0x} - p_x^{\text{trial}})(p_{0y} + p_y^{\text{trial}}) \tag{90}$$

and checking (sign will change depending on the orientation of the yield function polyline)

$$\begin{cases} Q < 0 & \text{elastic (clockwise orientation)} \\ Q > 0 & \text{plastic (counter-clockwise orientation)}\,. \end{cases} \tag{91}$$

Since the plastic part of the stress-update algorithm also requires a closest point calculation in z and r'-space, the procedure for evaluating the yield condition discussed above should be carried out in that space for efficiency. Once the closest point has been found and transformed back into p-$\sqrt{J_2}$ space, the stress tensor at that point can be computed using

$$\boldsymbol{\sigma}^c = p^c \boldsymbol{I} + \frac{\sqrt{J_2^c}}{\sqrt{J_2^{\text{trial}}}} \boldsymbol{s}^{\text{trial}} \tag{92}$$

where the superscript c indicates quantities at the closest point and the superscript "trial" indicates the corresponding trial stress values.

The stress update process also requires the computation of the yield surface normal at the closest point. The composite yield function is

$$f = \sqrt{J_2} - h(p) \tag{93}$$

and the normal is given by

$$\boldsymbol{N} = \frac{\partial f}{\partial \boldsymbol{\sigma}} = \frac{\partial f}{\partial p}\frac{\partial p}{\partial \boldsymbol{\sigma}} + \frac{\partial f}{\partial J_2}\frac{\partial J_2}{\partial \boldsymbol{\sigma}} = \frac{\partial f}{\partial p}\frac{\partial p}{\partial \boldsymbol{\sigma}} + \frac{\partial f}{\partial J_2}\frac{\partial J_2}{\partial \mathbf{s}} : \frac{\partial \mathbf{s}}{\partial \boldsymbol{\sigma}}\,. \tag{94}$$

Since $p = 1/3\ \boldsymbol{I} : \boldsymbol{\sigma}$, $\boldsymbol{s} = (\mathbf{I} - 1/3 \boldsymbol{I} \otimes \boldsymbol{I}) : \boldsymbol{\sigma}$, and $J_2 = 1/2\ \boldsymbol{s} : \boldsymbol{s}$, we have

$$\frac{\partial p}{\partial \boldsymbol{\sigma}} = \tfrac{1}{3}\boldsymbol{I}\,, \quad \frac{\partial \boldsymbol{s}}{\partial \boldsymbol{\sigma}} = \mathbf{I} - \tfrac{1}{3}\boldsymbol{I} \otimes \boldsymbol{I}\,, \quad \frac{\partial J_2}{\partial \boldsymbol{s}} = \boldsymbol{s}\,. \tag{95}$$

Therefore,

$$\boldsymbol{N} = \frac{\partial f}{\partial p}\boldsymbol{I} + \frac{\partial f}{\partial J_2}\boldsymbol{s} = -\frac{dh}{dp}\boldsymbol{I} + \frac{1}{2\sqrt{J_2}}\boldsymbol{s}\,. \tag{96}$$

At the closest point, the tangent is $\mathbf{t}^c = (t_x^c, t_y^c)$ and we have

$$\frac{dh}{dp} = \frac{t_y^c}{t_x^c} \quad \text{and} \quad \boldsymbol{s} = \frac{\sqrt{J_2^c}}{\sqrt{J_2^{\text{trial}}}} \boldsymbol{s}^{\text{trial}}\,. \tag{97}$$

The normal at the closest point is therefore given by

$$\boldsymbol{N}^c = -\frac{t_y^c}{t_x^c}\boldsymbol{I} + \frac{1}{2\sqrt{J_2^c}}\frac{\sqrt{J_2^c}}{\sqrt{J_2^{\text{trial}}}}\boldsymbol{s}^{\text{trial}} = -\frac{t_y^c}{t_x^c}\boldsymbol{I} + \frac{1}{2\sqrt{J_2^{\text{trial}}}}\boldsymbol{s}^{\text{trial}}\,. \tag{98}$$

Thus we have all the quantities needed for the elastic-plastic stress update algorithm. The projection directions for determining the closest point and the normals to the yield surface at these points are shown in Figure 9. The two-dimensional plot in Figure 9(b) shows that the normals to the yield surface do not necessarily appear to be perpendicular to the yield function in p-$\sqrt{J_2}$ space, which is not the case when they are plotted in principal stress space (Figure 9(a)).

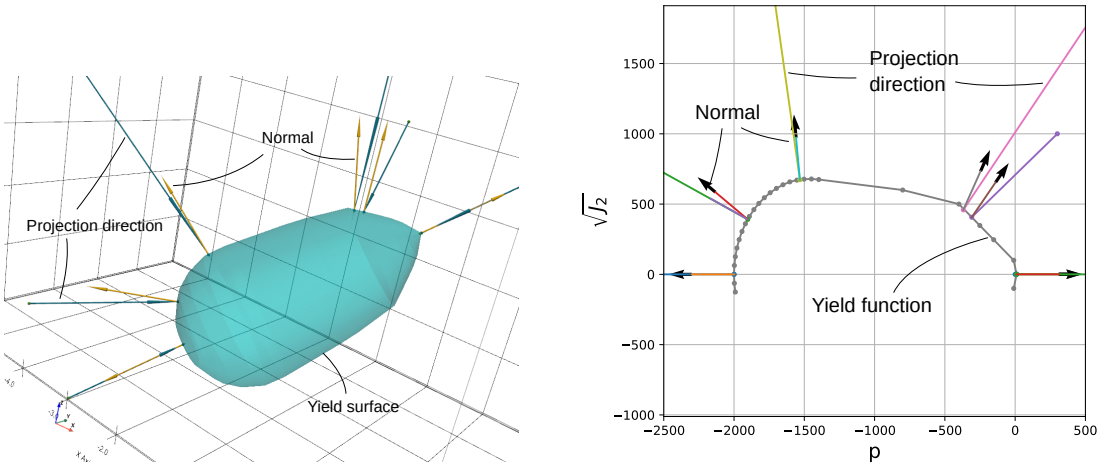

(a) Principal stress space.

(b) p-$\sqrt{J_2}$ stress space.

Figure 9 – *Projection directions and normals to the yield surface at the closest point from a trial value of stress. Note that these directions are generally not identical.*

6 Model response

The approach discussed in this work has been implemented in Vaango (Banerjee, 2014).[2] To verify the overall implementation, the suite of tests suggested by Kamojjala et al. (2015) were performed on single particles by driving the simulation with a prescribed deformation gradient time history. To check the validity of the tabular models of the poorly-graded sand, a single-particle hydrostatic compression test was simulated and compared with the experimental data. Model responses were also computed for uniaxial compression and simple shear using the sand tabular data.

6.1 Hydrostatic compression

The hydrostatic compression simulation was driven by a deformation gradient computed from volumetric strains in the loading-unloading curves of the poorly-graded concrete sand. The strains in the experimental curves were assumed to be logarithmic strains, related to the deformation gradient, $\boldsymbol{F} = \boldsymbol{R}\boldsymbol{U}$, by $\boldsymbol{\varepsilon} = \ln(\boldsymbol{U})$ where $\boldsymbol{U}$ is the stretch tensor and $\boldsymbol{R}$ is the rotation tensor. Figure 10(a) shows the deformation gradient time history, while Figure 10(b) shows the evolution of stress components as a function of time.

[2] The model can be accessed in Vaango using the material tag tabular_plasticity_cap. The elastic modulus model is invoked with the tabular_bulk tag, the yield condition model with tabular_cap, and the cap evolution model is activated with the internal variable model tag tabular_cap.

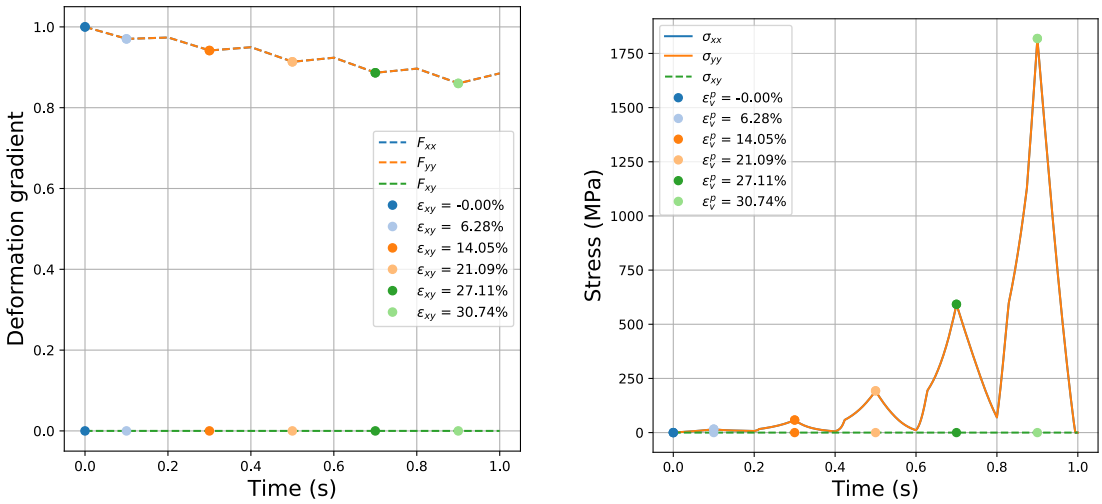

(a) Deformation gradient vs. time.

(b) Stress vs. time.

Figure 10 – *The deformation gradient used to drive the hydrostatic compression test, and the computed stress-time histories.*

A comparison of the experimental hydrostatic stress-strain curve with simulation results is shown in Figure 11(a). The figure also shows the pressures as functions of the volumetric elastic and plastic strains (ε_v^e, ε_v^p). Dashed lines indicate experimental data. Though the unloading points are simulated exactly as per the experiments and the cap crush-curve is also followed accurately, the predicted pressure starts to deviate from experiment at around 25% volumetric strain. The unloading bulk moduli are observed to be smaller that the experimental values when unloading at a volumetric strain of 36%. The discrepancy in final pressure can also be observed from the evolution of the yield surface in p-q–space, presented in Figure 11(b). The experimentally observed maximum value of the cap is more than two times the predicted value.

After careful examination of the implementation and verification of individual components of the model we were convinced that the implementation and approach were reasonable. The discrepancy between experiments and simulation could only be explained if the assumptions used to determine the plastic strains, bulk moduli, and cap pressures from the experimental data were not true. This includes the additive decomposition of strains into elastic and plastic parts, the assumption that plastic strains remain constant during unloading, and that the crush-curve plastic strains could be interpolated based on the elastic strains at the beginning of unloading. These issues require further investigation using micromechanical methods.

In the absence of improved theories of sand behavior, and to satisfy the need for efficient predictive models, we can scale the bulk modulus and cap pressure to fit observations as is usually done while fitting material models. If the bulk modulus is scaled by a factor of 1.7 and the crush-curve pressure is scaled by a factor of 1.2, we observe the results shown in Figure 12 (a) and (b). The elastic strain is considerably larger even though the effect on plastic strains is small, and the simulations match experimental data quite well. Better fits can, of course, be obtained using nonlinear optimization tools.

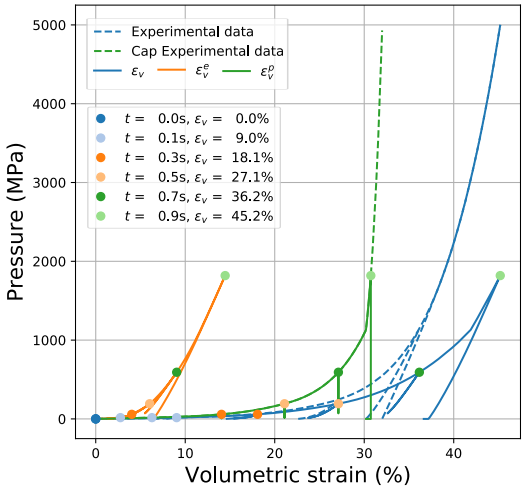

(a) Mean stress vs. volumetric strain.

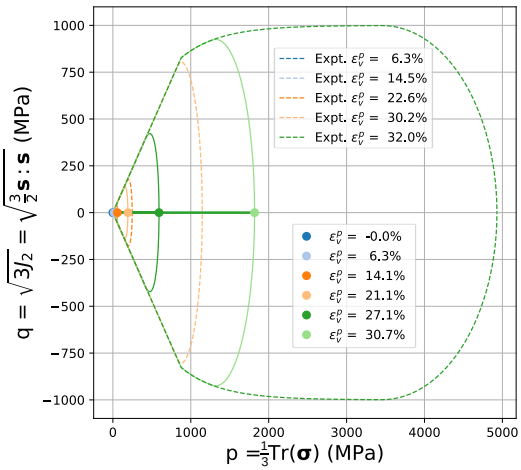

(b) Evolution of yield surface in p-q–space.

Figure 11 – *Evolution of stress and the yield surface in hydrostatic compression. Dashed lines indicate experimental values.*

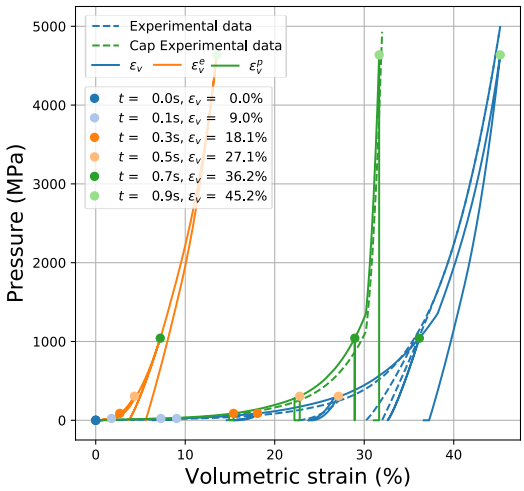

(a) Mean stress vs. volumetric strain.

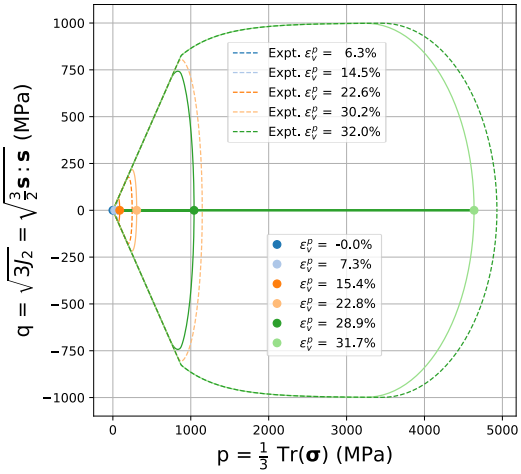

(b) Evolution of yield surface in p-q–space.

Figure 12 – *Effect of scaling the bulk modulus and cap pressure on the evolution of stress/yield surface in hydrostatic compression. Dashed lines indicate experimental values.*

6.2 Uniaxial strain compression

The behavior of the model in uniaxial strain, with scaled values of bulk modulus and compression cap, has been simulated for the strain history shown in Figure 13(a). It produces the stress-time response in Figure 13(b). The material is compressed to around 51% strain and then uncompressed until the stresses are zero. Notice that, beyond 38% axial strain, the model produces almost identical stresses in the x and y directions.

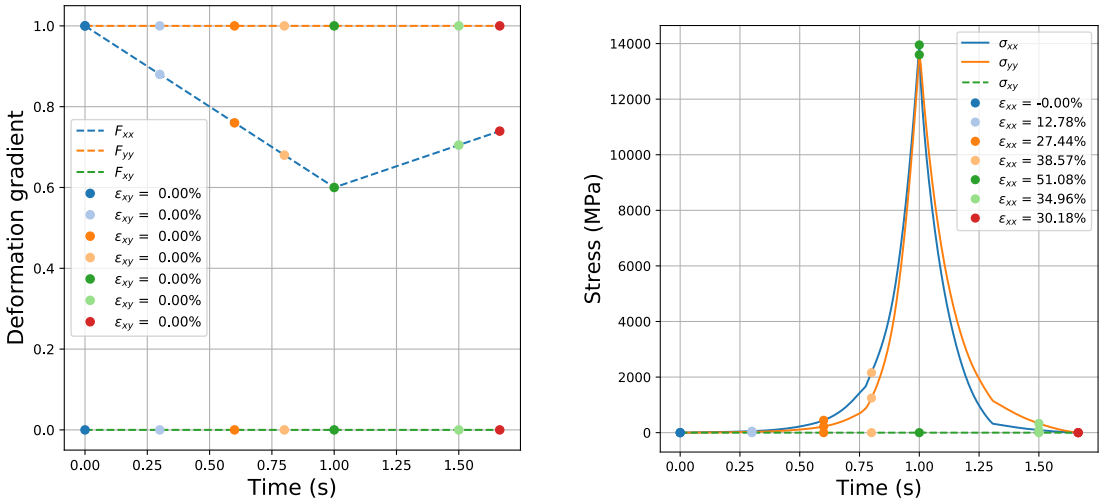

(a) Deformation gradient vs. time.

(b) Stress vs. time.

Figure 13 – *The deformation gradient used to drive the uniaxial compression test, and the compute stress-time evolution.*

The σ_{xx} and σ_{yy} components of stress are plotted as a function of the uniaxial strain in Figure 14(a). Expressed as a p-q plot, the stress path can be more readily visualized from Figure 14(b). The stress is approximately parallel to the initial yield surface up to a plastic strain of around 33% after which it turns towards the cap. During unloading, the stress follows an elastic path until it meets the yield surface. Further unloading is along the yield surface until the tension vertex is reached.

6.3 Simple shear deformation

A simple shear can be used to test the response of the model for a situation where the cap does not evolve. We used the scaled moduli and cap pressure, and the deformation gradient history shown in Figure 15(a) to simulate simple shear. The corresponding stresses have been plotted as a function of time in Figure 15(b). The shear stress rapidly reaches the yield surface, after which it follows the surface and drops to a negative value when unloading begins. The model predicts a normal stress that is approximately twice the shear stress in magnitude.

To determine whether the results in the previous figure are reasonable, we can examine the strain evolution plots shown in Figure 16. Elastic shear strains are small and the normal components sum to zero, as expected. The elastic shear strain increases to 0.01% before decreasing slightly. The trend is reversed during unloading. Plastic shear strains, on the other hand, are quite significant and increase

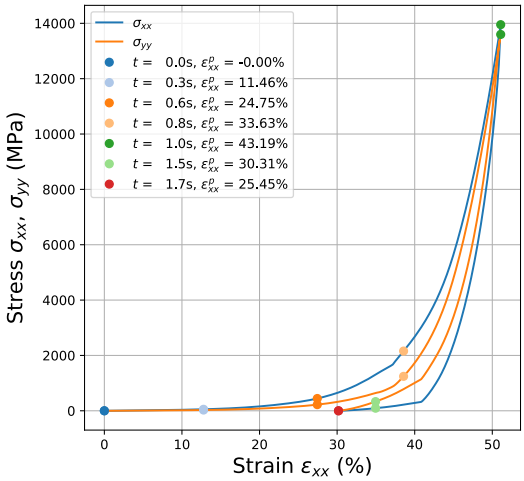

(a) Stress vs. strain in the compression direction.

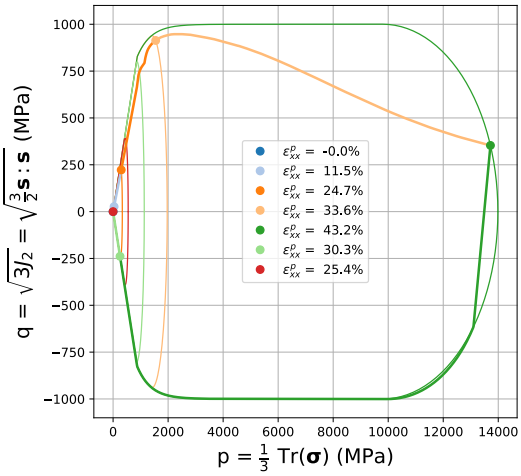

(b) Evolution of yield surface in p-q–space.

Figure 14 – *Evolution of stress and the yield surface in uniaxial strain compression. Dashed lines indicate experimental values.*

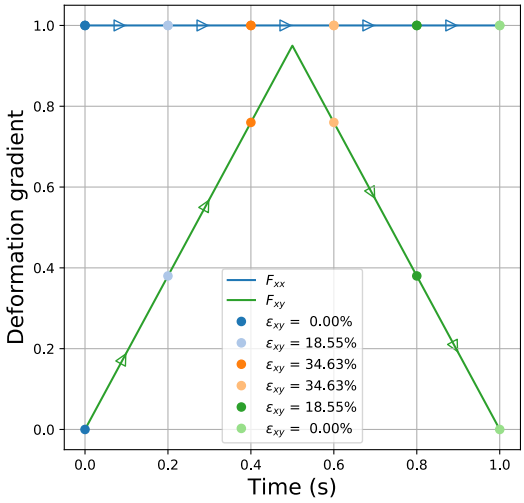

(a) Deformation gradient vs. time.

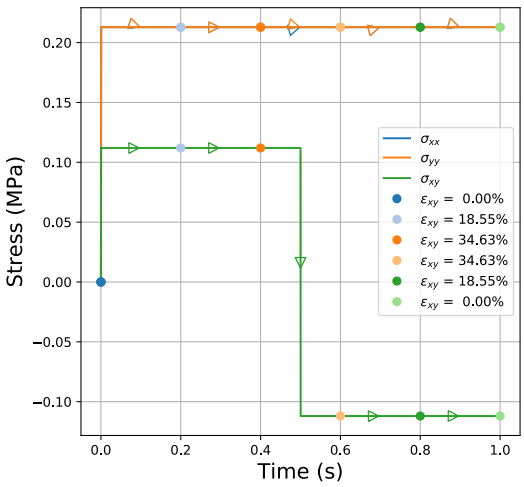

(b) Stress vs. time.

Figure 15 – *The deformation gradient used to drive the simple shear test, and the computed stress-time evolution.*

to around 40% before decreasing to zero at the end of unloading. Plastic normal strains are also non-zero but cancel out, leading to zero volumetric plastic strain during the entire load-unload cycle.

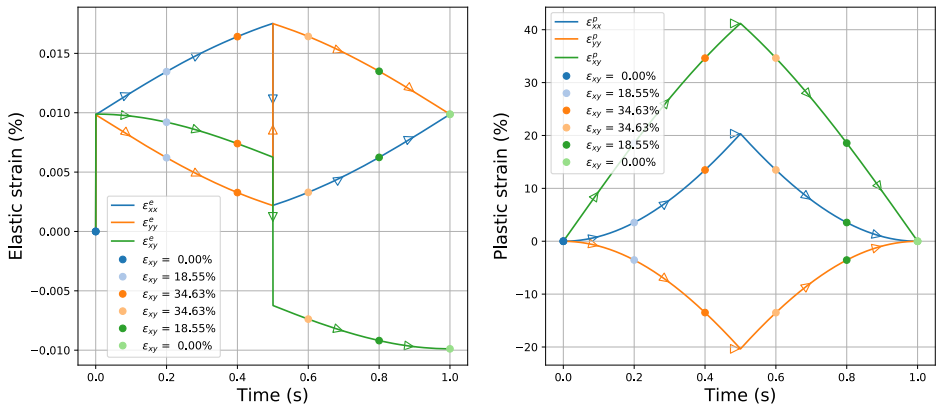

Figure 16 – *The evolution of strain tensor components in the simple shear test.*

Figure 17(a) shows a plot of the shear stress as a function of the shear strain (ε_{xy}). The rapid change in the shear stress indicates that the material does not resist shear and deforms rapidly under shear strains. The same behavior can be observed in the yield surface plot shown in Figure 17(b). The stress state cannot go into the cap region of the model and remains at the top of cap. The plot also shows that a small amount of volumetric plastic strain is computed by the model, possibly due to numerical imprecision.

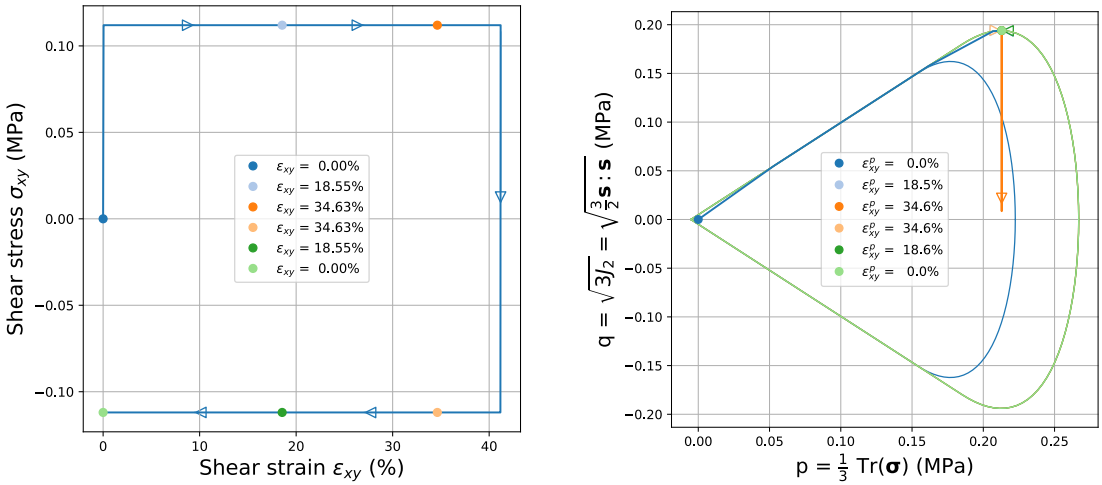

(a) Stress vs. strain in the compression direction. (b) Evolution of yield surface in p-q–space.

Figure 17 – *Evolution of stress and the yield surface in uniaxial strain compression. Dashed lines indicate experimental values.*

7 Concluding remarks

The algorithm described in this work involves a number of table searches at each timestep of an simulation. The search process is considerably sped up when a kd-tree is used, particularly at high pressures when the yield surface can easily contain several thousand discretization points. We have observed that speed improvements of the order of 5-10 times over the course of a simulation when kd-trees are used, even when the index is recomputed for each closest point calculation, than when linear searches of the yield function or bulk modulus tables are used.

Improved estimates of the unloading paths during hydrostatic compression are produced when the elastic moduli data are input in the form of bulk modulus vs. pressure data, rather than as bulk modulus vs. strain tables. This is partly because the stress state on the yield surface is geometrically accurate and elastic strains are computed on the basis of the stress state. While pressure vs. total strain curves could have been used instead, we have shown (Banerjee, Fox, and Regueiro, 2020a) that the interpolated moduli are less accurate in that case and also produce steeper unloading curves.

The elastic-plastic coupling term ($\boldsymbol{Z}$) typically contributes around 1% to the value of the projection tensor $\boldsymbol{P}$. However, at high pressures the value of derivative of the bulk modulus with respect to plastic volumetric strains becomes large, such that $\boldsymbol{Z} \geq \mathbf{C} : \boldsymbol{M}$. As a result $\boldsymbol{P}$ switches direction and can cause the computed value of Γ, the plastic strain rate factor, to become negative. Since the effect of the coupling term is small when we use the iterative algorithm with small timesteps discussed in this paper, we ignore that terms in our calculations.

Another effect that is observed is that the iterations for Γ_F may fail to converge near regions of large curvature in the yield surface. A bisection algorithm such as that discussed in previous work (Banerjee and Brannon, 2017; Banerjee and Brannon, 2019) can be used to produce more accurate results in these regions of stress space. However, the overall effect on the final solution has not been found to be significant enough to justify the extra computation work needed.

The most significant physical observation from this study is that the assumptions that were used to extract the bulk modulus and crush curve from experimental data may not be accurate, as exhibited by the failure to reproduce experimental hydrostatic compression data without increasing the bulk modulus and cap pressure. This indicates that these assumptions need to be re-examined, particularly the assumption of continued isotropy of the material upon compressive loading and unloading.

Acknowledgements

This research has been partially funded by the US Office of Naval Research PTE Federal award number N00014-17-1-2704.

References

Banerjee, B. (2014). *Vaango User Manual: parallel simulation of high strain-rate solid mechanics with the Material Point Method*. https://github.com/bbanerjee/ParSim/tree/master/Vaango (cit. on p. 20).

Banerjee, B. and R. M. Brannon (2017). *Theory, verification, and validation of the ARENA constitutive model for applications to high-rate loading of fully or partially saturated granular media*. Tech. rep. PAR-10021867-1516.v1. Parresia Research Limited and University of Utah. DOI: 10.13140/RG.2.2.10671.53922 (cit. on p. 26).

— (2019). "Continuum modeling of partially saturated soils". In: *Shock Phenomena in Granular and Porous Materials*. Ed. by T. Vogler and A. Fredenburg. Springer (cit. on pp. 5, 26).

Banerjee, B., D. M. Fox, and R. A. Regueiro (2020a). *Interpolating tabular data for granular material models*. Tech. rep. PAR-10021867-092020-3. Parresia Research Limited (cit. on pp. 2, 5, 15, 26).

— (2020b). *Multilayer perceptron neural networks as multi-variable material models*. Tech. rep. PAR-10021867-092020-2. Parresia Research Limited (cit. on p. 2).

— (2020c). *Support vector regression for fitting multi-variable material models*. Tech. rep. PAR-10021867-092020-1. Parresia Research Limited (cit. on p. 2).

Blanco, Jose Luis and Pranjal Kumar Rai (2014). *nanoflann: a C++ header-only fork of FLANN, a library for Nearest Neighbor (NN) with KD-trees*. https://github.com/jlblancoc/nanoflann (cit. on p. 17).

Brannon, R. M. (2007). "Elements of phenomenological plasticity: geometrical insight, computational algorithms, and topics in shock physics". In: *ShockWave Science and Technology Reference Library*. Springer, pp. 225–274 (cit. on pp. 5, 7, 9, 12, 15).

Brannon, R. M., T. J. Fuller, et al. (2015). "KAYENTA: Theory and User's Guide". In: *Sandia National Laboratories report SAND2015-0803* (cit. on pp. 3, 6).

Brannon, R. M. and S. Leelavanichkul (2010). "A multi-stage return algorithm for solving the classical damage component of constitutive models for rock, ceramics, and other rock-like media". In: *International Journal of Fracture* (cit. on p. 13).

Feito, F, Juan Carlos Torres, and A Urena (1995). "Orientation, simplicity, and inclusion test for planar polygons". In: *Computers & Graphics* 19.4, pp. 595–600 (cit. on p. 19).

Fox, D. M. et al. (2014). "The effects of air filled voids and water content on the momentum transferred from a shallow buried explosive to a rigid target". In: *International Journal of Impact Engineering* 69, pp. 182–193 (cit. on p. 2).

Gordon, William J and Richard F Riesenfeld (1974). "B-spline curves and surfaces". In: *Computer aided geometric design*. Elsevier, pp. 95–126 (cit. on p. 17).

Homel, Michael A (2015). "Elastoplastic constitutive modeling of fluid-saturated porous materials with new methods for numerical solution and mesoscale validation". PhD thesis. The University of Utah (cit. on p. 12).

Hueckel, T and G Maier (1977). "Incremental boundary value problems in the presence of coupling of elastic and plastic deformations: a rock mechanics oriented theory". In: *International Journal of Solids and Structures* 13.1, pp. 1–15 (cit. on p. 8).

Kamojjala, K. C. et al. (2015). "Verification tests in solid mechanics". In: *Engineering with Computers* 2, pp. 193–213 (cit. on p. 20).

Simo, Juan C and Thomas JR Hughes (2006). *Computational inelasticity*. Vol. 7. Springer Science & Business Media (cit. on p. 12).